Nanoscale

Accepted Manuscript

Volume 10
Number 4
28 January 2018
Pages 1549-2172

Nanoscale

rsc.li/nanoscale

ISSN 2040-3372

PAPER
Shuping Xu, Chongyang Liang et al.
Organelle-targeting surface-enhanced Raman scattering (SERS) nanosensors for subcellular pH sensing

NCNST

This is an Accepted Manuscript, which has been through the Royal Society of Chemistry peer review process and has been accepted for publication.

Accepted Manuscripts are published online shortly after acceptance, before technical editing, formatting and proof reading. Using this free service, authors can make their results available to the community, in citable form, before we publish the edited article. We will replace this Accepted Manuscript with the edited and formatted Advance Article as soon as it is available.

You can find more information about Accepted Manuscripts in the Information for Authors.

Please note that technical editing may introduce minor changes to the text and/or graphics, which may alter content. The journal's standard Terms & Conditions and the Ethical guidelines still apply. In no event shall the Royal Society of Chemistry be held responsible for any errors or omissions in this Accepted Manuscript or any consequences arising from the use of any information it contains.

ROYAL SOCIETY
OF CHEMISTRY

rsc.li/nanoscale

Journal Name

ARTICLE

Induced Ferroelectric Phases in SrTiO₃ by a Nanocomposite Approach

Erik Enriquez,[†,a,b] Qian Li,[†,c] Pamela Bowlan,[a] Ping Lu,[d] Bruce Zhang,[e] Leigang Li,[e] Haiyan Wang,[e] Antoinette J Taylor,[a] Dmitry Yarotski,[a] Rohit P. Prasankumar,[a] Sergei V. Kalinin,[f] Quanxi Jia,[g] Aiping Chen[*,a,b]

Inducing new phases in thick films via lattice strain is one of the critical advantages of vertically aligned nanocomposites (VANs). In SrTiO₃ (STO), the ground state is ferroelastic, and the ferroelectricity in STO is suppressed by the orthorhombic transition. Here, we explore whether vertical lattice strain in three-dimensional VANs can be used to induce new ferroelectric phases in SrTiO₃:MgO (STO:MgO) VAN thin films. The STO:MgO system incorporates ordered, vertically aligned MgO nanopillars into a STO film matrix. Strong lattice coupling between STO and MgO imposes a large lattice strain in the STO film. We have investigated ferroelectricity in the STO phase, existing up to room temperature, using piezoresponse force microscopy, phase field simulation and second harmonic generation. We also serendipitously discovered the formation of metastable TiO nanocores in MgO nanopillars embedded in the STO film matrix. Our results emphasize the design of new phases via vertical epitaxial strain in VAN thin films.

1. Introduction

Strain engineering provides tremendous opportunities in fundamental research and technological applications for epitaxial thin films.[1-5] Vertically aligned nanocomposite (VAN) thin films with two phases epitaxially grown on a substrate extend conventional strain engineering via the substrate to vertical strain engineering via vertical interface couplings between these two epitaxially grown phases.[6, 7] Vertical strain engineering provides unique advantages to tune the functional properties of thick films.[8, 9] Strain in both lateral heterostructures and VANs has thus been used to tune ferroelectricity,[9-12] superconductivity,[13, 14] magnetic anisotropy,[15, 16] and magnetotransport.[8, 17] Beyond strain tuning of bulk physical properties, the growth process in VANs can induce structural and chemical changes including symmetry breaking at vertical interface, defects, and microstructure modulation. Some of them have been

used to tune functionalities in VANs.[7, 18-22] For example, oxygen vacancies at the vertical interfaces could serve as both electronic and ionic conduction pathways.[23-26] These phenomena could be used to design high-density memory devices,[27, 28] and solid oxide fuel cells.[29, 30] The interplay between strain tuning of physical properties and strain relaxation through structural and chemical changes has been extensively explored in classical lateral heterostructures.[31-36] For example, it was reported that defect formation (e.g., cation or oxygen vacancies) and microstructure modulation are coupled with strain relaxation in thin films.[37-39] However, strain-defect-microstructure-function correlation in VANs is not well-established. It is therefore critical to know how strain, defect, microstructure and functional properties are connected in VANs.

To explore this critical question, a model system of SrTiO₃:MgO (STO:MgO) with a large lattice mismatch is designed, as shown in Figure 1. STO is a centrosymmetric quantum paraelectric material. The large quantum fluctuations at low temperatures and antiferrodistortive transition in STO suppresses ferroelectric instabilities and prevents the ferroelastic phase from becoming ferroelectric, though it was reported that terahertz pulses can induce a metastable ferroelectric phase and epitaxial strain can be used to stabilize a ferroelectric phase in STO.[40, 41] MgO is a stable insulating oxide without significant non-stoichiometry or phase transitions. In addition, STO is a cubic perovskite with a lattice parameter of 3.905 Å, and cubic MgO has a lattice parameter of 4.212 Å. A large lattice mismatch of ~7% is anticipated in STO:MgO VANs. Conventional strain engineering has demonstrated that such a large lattice mismatch usually favors domain-matching epitaxy, as observed in MgO/STO (or STO/MgO) heterostructures.[42] In VANs, this large

a. Center for Integrated Nanotechnologies (CINT), Los Alamos National Laboratory, Los Alamos, New Mexico 87545, USA
b. Institute for Materials Science, Los Alamos National Laboratory, Los Alamos, NM 87545, USA
c. State Key Laboratory of New Ceramics and Fine Processing, School of Materials Science and Engineering, Tsinghua University, Beijing 100084, China
d. Sandia National Laboratories, Albuquerque, New Mexico 87185, USA
e. School of Materials Engineering, Purdue University, West Lafayette, Indiana 47907, USA
f. Center for Nanophase Materials Sciences and Institute for Functional Imaging of Materials, Oak Ridge National Laboratory, Oak Ridge, TN, USA
g. Department of Materials Design and Innovation, University at Buffalo - The State University of New York, Buffalo, NY 14260, USA
† These authors contributed to this work equally.
* Email: apchen@lanl.gov

Electronic Supplementary Information (ESI) available: [details of any supplementary information available should be included here]. See DOI: 10.1039/x0xx00000x

ARTICLE

mismatch could be used to design a large strain via direct lattice matching at vertical interfaces, as previously observed in the $La_{0.7}Sr_{0.3}MnO_3$:MgO system.[8] Therefore, this system allows us to study strain-induced new ferroelectric phases and other functional properties in this system.
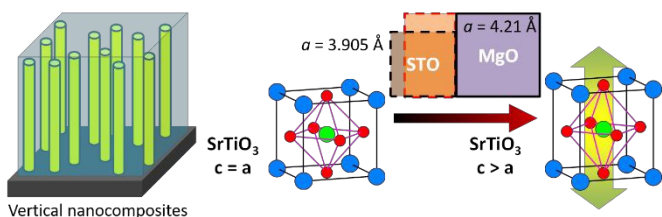

Figure 1. Design of STO:MgO vertical heteroepitaxial nanocomposites with induced large tetragonality in the STO phase.

Here, STO:MgO (35% in volume) thin films have been grown on STO substrates. The microstructure is carefully investigated by high-angle annular dark-field imaging (HAADF) scanning transmission electron microscopy (STEM). The vertical strain-induced ferroelectricity in the STO film matrix is investigated by piezoresponse force microscopy (PFM), phase field simulation and second harmonic generation (SHG). Our results demonstrated that VAN thin films is a unique approach to design large lattice strain and achieve strain-induced new functional properties.

2. Results and Discussion

Strain engineering and nanocomposite film growth

Figure 2a shows the ω-2θ scan of STO:MgO thin films on STO substrates grown at 700 °C. The STO film peak deviates significantly from the STO substrate towards a lower angle. The out-of-plane lattice parameter ($a_\perp$) of the STO phase is increased to 3.964 Å, compared to bulk STO (a_0 = 3.905 Å), corresponding to an out-of-plane strain of 1.5%. in the contrary, the MgO peak shifts towards a higher angle, and the out-of-plane lattice parameter of MgO phase decreases to 4.110 Å, corresponding to a compressive strain of -2.4%. MgO exerts out-of-plane tensile stress to the STO phase, while STO conversely exerts compressive stress to the MgO phase. The strain state in the STO phase is confirmed by reciprocal space map (RSM). Figure 2b shows the RSM scans around the STO (113) peak. It is clear that the STO phase is not fully strained to the STO substrate. The in-plane lattice parameter ($a_\parallel$) of the STO phase is slightly reduced to ~3.890 Å and an out-of-plane strain is estimated to be 1.5%. It has been reported that the out-of-plane lattice parameter of perovskite oxide thin films such as STO and $BaTiO_3$ also strongly depends on the cation stoichiometry which is affected by growth conditions.[33, 43, 44] Indeed, defect formation (e.g., oxygen vacancy and cation off-stoichiometry) and microstructure modulation have been reported to accommodate the large lattice mismatch. To investigate the origin of the out-of-plane lattice parameter variation in STO film matrix, we selectively etched the MgO pillars and investigated the STO peak shift. For a STO:MgO VAN film grown at 800 °C, the out-of-plane lattice parameter of the STO matrix is 3.928 Å. After etching away the MgO nanopillars, the STO film peak relaxes to 3.911 Å, indicating an elastic coupling between STO and MgO pillars.[7] The deviation of the STO peak after etching could be related to a slight cation off-stoichiometry. The cation stoichiometry is responsible for 25% of

lattice parameter variation while vertical lattice coupling is responsible for 75% of lattice change. Therefore, except the elastic deformation, Vegard expansion of the lattice caused by defects (such as cation off stoichiometry) also contributes to the large out-of-plane lattice parameter in the STO film matrix of the VAN.[45] From the relationship between Sr stoichiometry and lattice parameter provided by Brook et al.,[43] we suspect that the VANs with 35% MgO pillars could exhibit 2-3% of Sr excess in the STO film matrix. However, the lattice parameter change in VANs dominates by the elastic vertical strain coupling and the slight cation stoichiometry also plays a role.

To study the microstructure of STO:MgO thin films, the HAADF-STEM images were collected. As shown in Figure 2c, the cross-sectional STEM image of STO:MgO thin film shows a clear phase separation with vertically and alternatively aligned MgO and STO phases on the substrate. The dark contrast represents MgO phase and white contrast represents STO phase. Figure 2d shows a plan-view STEM image of the same film. It can be seen that both square and rectangular MgO features are evenly distributed in the STO matrix with a pillar size of 5-10 nm. Figure 2e shows a plan-view high-resolution-STEM (HR-STEM) image with one MgO pillar in the STO matrix. The rectangular MgO shape with faceted edge evolves as the result of the competition between strain energy and surface energy. The STO:MgO thin film exhibits well-defined vertically aligned nanocomposite (VAN) structure with vertical MgO nanopillars embedded in epitaxial STO film matrix. Therefore, the STO:MgO VAN is highly strained and MgO nanopillars are ordered in the STO film matrix.
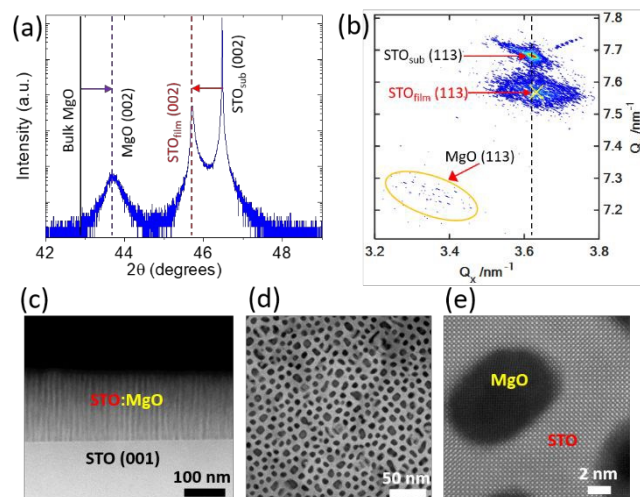

Figure 2. (a) ω-2θ XRD scan of STO:MgO VAN thin films grown at 700 °C with 35% MgO in volume. (b) RSM of the STO:MgO VAN around the STO (113) peak. HADDF-STEM of (c) cross-sectional and (d) plan-view images of STO:MgO VAN on STO substrate. (e) HR-STEM plan-view image showing one MgO nanopillar in the STO matrix.

Strain relaxation mechanisms in STO:MgO VANs

To understand strain relaxation mechanisms in STO:MgO VAN with the large lattice mismatch, plan-view STEM images are further analyzed. Figure 3a is a plan-view HR-STEM image, showing the

distribution of MgO nanopillars in the STO matrix. Unexpectedly, larger MgO nanopillars contain another phase inside of the nanopillars. STEM energy-dispersive x-ray spectroscopy (EDS) mapping, as shown in Figure 3b, indicates the presence of Ti in the center of MgO nanopillars. This observation implies the formation of TiO_x nanopillar core in MgO shell when the MgO pillar size is large. We speculate that the pillar core is rock salt TiO phase (lattice constant 4.17 Å), which is extremely similar to the rock salt MgO in terms of both crystal structure and lattice constant. Furthermore, TiO exhibits a metastable superconducting phase when previously grown on Al_2O_3 substrates.[46] Our work indicates that MgO could be an ideal substrate to stabilize the metastable TiO phase and tune the superconducting properties by strain and stoichiometry. On the other hand, the formation of TiO core in MgO pillars also indicates the deficiency of Ti in the STO film matrix, which could be related to the inelastic components for the STO lattice parameter.

To analyze the core-shell structure formation mechanism, the relative distribution of pillar size based on a random sampling of 500 nanopillars is shown in Figure 3c. The distribution centers on a nanopillar diameter of ~7 nm. It is interesting that a core-shell structure with the TiO core in the MgO shell tends to form when MgO nanopillars are greater than ~9 nm in diameter. The formation of the TiO/MgO core-shell structure in the STO matrix could be one of the main mechanisms for strain relaxation in regions with bigger MgO pillars. As known, the microstructure is a result of the minimization of total free energy, which is the sum of its surface and elastic energies.[7] The ratio of elastic to surface energy for the second phase is proportional to its size.[47] Larger MgO pillar diameter significantly increases the strain energy over surface energy. The formation of the TiO/MgO core-shell structure reduces the effective size of MgO pillars and decreases the elastic energy of MgO pillars, which minimizes the total free energy of the STO:MgO VAN.
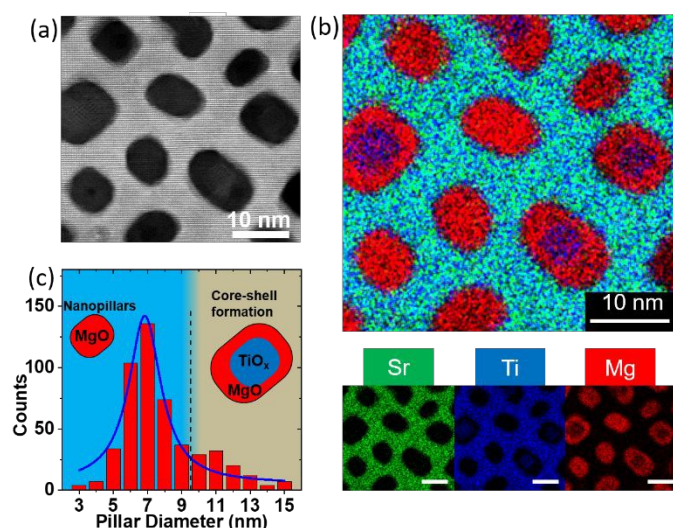
Strain induced ferroelectricity in STO:MgO VANs

The incorporation of MgO nanopillars in the STO matrix produces significant out-of-plane strain in the STO phase, and such strain could dramatically modify the properties of STO. To explore strain induced ferroelectricity theoretically, we have performed phase-field modeling based on the fully-coupled Landau-Ginzburg theory (see Method for details).[48-50] In particular, the realistic microstructure observed by HAADF-STEM has been adopted in the model to reproduce the strain state of the STO:MgO VAN with high veracity. Figure 4a illustrates the spatial distributions of the out-of-plane strain (with reference to the lattice parameter of bulk STO), ε_{zz}, and polarization, P_z. The ε_{zz} is largely homogeneous within both phases across the film thickness except for the near-surface and substrate regions. Figure 4b presents the histograms of the strain and polarization field variables in the simulated box. The calculated strain values are in agreement with the XRD results, with a slight overestimate (~1.9% vs 1.5%) for ε_{zz} in the STO phase. This can be due to the reason that we have assumed coherent vertical MgO/STO interfaces, without accounting for possible strain relaxation. Due to this tensile strain, an appreciable polarization of ~12 μC/cm^2, as shown in Figure 4c, is induced within the STO matrix along [001] (the polarization along the [100]/[010] is negligible), while laterally, this polarization shows fluctuations depending on the vicinity and local density of MgO pillars. It is known that there is a competition between FE transition, orthorhombic transition and quantum critical fluctuations in STO. The lattice strain in STO matrix imposed by MgO pillars destabilizes the zone boundary soft phonon modes and thus promotes the ferroelectric transition.

To explore the potential emergence of functionalities related to zone boundary modes, piezoresponse force microscopy (PFM) has been employed to further confirm the existence of ferroelectricity in the STO:MgO VAN thin films. Figures 4d and 4e show typical surface morphology and PFM image of this VAN film. Grainy features with characteristic sizes of 40-50 nm are observed, and correlated with this morphology, the surface piezoresponse is rather non-uniform. Generally, those protruding regions exhibit much higher piezoresponse, suggesting larger out-of-plane strains. The majority of the surface region has well-defined local switching behavior, as illustrated by the switching loop area (a measure of switchable polarization) and selected hysteresis loops (Figures 4f and 4g). Aside from the variations in magnitude, all the measured loops appear to be symmetric and saturate at high applied voltages, which again, points to an inhomogeneous polarization state primarily associated with local strain relaxation and MgO pillar distribution. We have also performed PFM on the STO:MgO VAN with 22% MgO (a vertical strain of ~1.0%). It shows piezoelectric response (not shown), but it is weaker than the VAN with 1.5% strain and the switching is not as well-defined as 1.5% strain sample. This confirms that a larger strain could help to establish polarization in the STO film matrix.
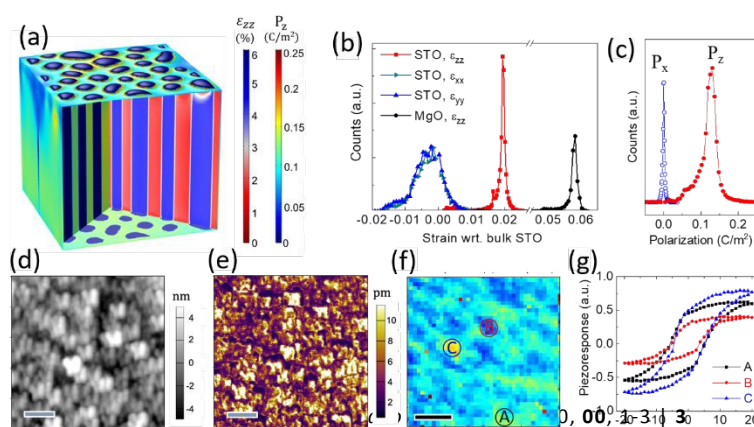

Figure 3. (a) HR-STEM image showing MgO pillars in $SrTiO_3$ matrix. (b) Top panel, a composite elemental map of Sr (green), Ti (blue) and Mg (red) of MgO pillars in $SrTiO_3$ matrix. Bottom panel, EDS map of Sr, Ti and Mg, respectively. (c) Size distribution of random sampling of 500 MgO pillars. The blue curve represents the fitting of pillar size by the Lorentz distribution.

Nanoscale Accepted Manuscript

ARTICLE

Journal Name

Figure 4. (a) The spatial distributions of the out-of-plane strain ε_{zz} , with respective to bulk STO lattice and polarization P_z in the STO:MgO VAN from phase field simulation. The histograms of the (b) calculated strain and (c) calculated polarization. (d) Surface morphology, (e) PFM image and (f) spatially resolved band-excitation polarization switching mapping of a VAN thin film with 35% of MgO pillars (1×1 μm²), measured at room temperature. The scale bar in (d), (e) and (f) is 200 nm. (g) piezoresponse vs. bias for the STO:MgO system at different locations in (f).

It is reported that the PFM signal can originate from both ferroelectricity and ionic activity of the surface. Optical SHG is further used to confirm the presence of ferroelectricity in STO:MgO VANs, since ferroelectric order produces a large second order polarization due to inversion symmetry breaking. The dependence of the measured SHG signal on the polarization of the input fundamental light can be used to extract the electronic and lattice symmetry.[51] 800 nm, 100 femtosecond (fs) amplified Ti:Sapphire laser pulses with a fluence of ~0.4 mJ/cm² and at a repetition rate of 250 kHz were incident at ~20° on the sample, which was placed in a continuous flow liquid He cryostat to control its temperature. The s and p-polarization components of the reflected 400 nm SHG signal were measured versus the input 800 nm pulse polarization. The STO substrate produces surface SHG as well as bulk SHG (not associated with FE order).[52] Therefore, to distinguish SHG from the substrate from SHG produced in the VAN films, we also measured the SHG signal from a bare STO substrate for comparison. It should be noted that microwave spectroscopy can be used to probe weak ferroelectric phase transitions.[53]
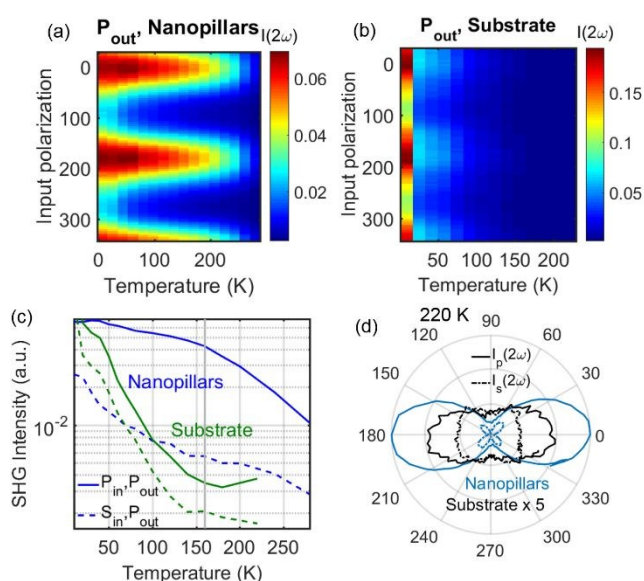

Figure 5. Optical SHG characterization of STO:MgO thin films. The reflected p-polarized SHG (at 400 nm), versus the input polarization of the fundamental field (800 nm), and the sample temperature for (a) the STO:MgO VAN films on the STO substrate and (b) a bare STO substrate. (c) Lines taken from the images in (a) and (b) showing the SHG intensity versus temperature. (d) The fundamental (or input) polarization dependence at 220 K for the s and p components of the SHG signal. In this figure, the signal for the substrate was scaled up 5 times for both s and p polarizations.

The results in Figures 5a and 5b show clear differences in the SHG from a bare STO substrate and the STO:MgO VAN film on a STO substrate. The VAN film produces significant SHG up to 270 K (the highest temperature measured), which slowly increases down to ~20 K, while the substrate has very little SHG at temperatures above 160 K. We only measured the SHG of the substrate up to 220 K, where its SHG became too weak to detect and no longer showed appreciable variation with increasing temperature. The SHG from the VANs continues to increase below 160 K, but with a different slope (blue line, Figure 5c). The SHG intensities versus input 800 nm pulse polarization in Figure 5d for the STO:MgO film and the bare substrate also have different shapes. This is indicative of different electronic symmetries, the latter most probably due to inversion symmetry breaking by the surface.

The most compelling signature of FE in the SHG signal from the STO:MgO film is the C_{4v} symmetry seen in Figures 5a and 5d. This is very similar to the symmetry that was previously measured in $Ba_{0.1}Sr_{0.9}TiO_3$ and strained STO films.[54, 55] This C_{4v} symmetry is usually associated with ferroelectricity in this family of oxides. The weak, high temperature (T >160 K) SHG from the bare substrate does not show the C_{4v} symmetry, and is instead surface SHG from the air/STO interface.[52] There is also information about the FE phase transition temperature in the temperature dependence of the SHG. We interpret the inflection in the P_{in}, P_{out} curve in Figure 5c at 160 K, as the Curie temperature (T_c) for the strained STO phase in the STO:MgO VANs. However, such a vertical strain induced ferroelectricity could exhibit large non-homogeneity.[11,56] Consistent with the non-uniform strain and the room temperature FE discussed above, this phase transition is very broad, and even at 270 K, far above T_c, a SHG signal indicating C_{4v} symmetry, or FE order, is still present. This large T_c distribution is also consistent with the non-uniformity of PFM data in Figure 4f, as well as reports that non-uniform strain creates a very large T_c distribution. The 160 K inflection is not seen in the measurement of the substrate; in fact, even at very low temperatures, down to 7 K, the STO substrate never displayed SHG with the C_{4v} symmetry seen in the STO:MgO VAN. Therefore, the combined PFM and SHG characterization has confirmed the presence of strain-driven ferroelectricity in the STO phase.

3. Conclusion

Epitaxial STO:MgO VAN thin films, consisting of MgO nanopillars embedded in a STO film matrix, have been synthesized. A large strain of ~1.5% is achieved in the STO film matrix. The enlarged lattice parameter is mainly attributed to the elastic strain coupling between MgO vertical nanopillars and STO film matrix while the Sr excess also plays a role. Vertical strain induces ferroelectricity in the STO phase, confirmed by both PFM and SHG characterization. The phase field simulation results indicate the non-uniform strain distribution, which is consistent with a location-dependent piezoelectric response and large T_c distribution in SHG. We also serendipitously discover that TiO nanocores are formed in the MgO nanopillars, which indicates that MgO could be an ideal substrate for the stabilization of a TiO superconducting phase. These results emphasize that large vertical strain is an effective approach to induce new phases in VAN thin films, and the discovered strain relaxation mechanisms could be beneficial to design other VAN systems with a large lattice mismatch.

4. Experimental section

Thin film growth. Epitaxial STO:MgO VAN thin films were grown on STO (001) and Nb:STO (001) substrates by PLD using a KrF excimer laser (Lambda Physik LPX 300, λ = 248 nm, 4 Hz, 2.0 J/cm^2). The STO:MgO composite targets used for the deposition was fabricated by a conventional ceramic sintering process with STO:MgO molar ratio of 35:65 and 50:50, and the volume ratio of MgO is about 35 % and 22%, respectively. The two particular MgO ratios are selected as the strain can be as large as 1.5% and 1.0%, respectively. Prior to the deposition, the chamber was pumped down to a base pressure of 1×10^{-6} Torr. A substrate temperature of 700°C and an oxygen pressure of 50 mTorr were maintained during all depositions. Both the target and the substrate are rotated during the deposition to achieve better uniformity, with an average growth rate of approximately 0.3 Å per laser pulse. After deposition, 500 Torr ultra-high purity O_2 and cooling at 5°C/min to 600°C, where the temperature was held for 1 hour. The film as then cooled down to room temperature at 5°C/min.

Structural characterization. X-ray diffraction (Panalytical X'Pert PRO MRD), using ω-2θ, and reciprocal space maps (RSM) was employed to obtain information on the orientation, lattice parameters and epitaxial quality of the thin films. Scanning transmission electron microscopy (HRSTEM) was used to investigate the film microstructure. A FEI Titan^{TM} G2 80-200 STEM with a Cs probe corrector and ChemiSTEM^{TM} technology (X-FEG^{TM} and SuperX^{TM} EDS with four windowless silicon drift detectors) operated at 200 kV was used in this study. The EDS spectral imaging was acquired by using an electron probe of size less than 0.13 nm, convergence angle of 18.1 mrad, and current of ~75 pA Elemental maps were extracted from the spectral imaging datasets with selected EDS energy windows for each element. High-angle annular dark-field (HAADF) images were recorded using an annular detector with a collection range of 60-160 mrad.

Piezoresponse force microscopy (PFM). PFM was carried out in ambient environment on a commercial atomic force microscope (Cypher AFM, Asylum Research), using Pt-coated conductive Si probes (Nanosensors PPP-EFM) with medium stiffness of 2–5 N m^{-1}. A tip loading force of ~300 nN was applied in the contact mode for all measurements. A home-built, Labview-based band excitation (BE) system consisting of a PXIe-6124 data acquisition card (National Instruments) was employed to perform BE switching spectroscopy. In BE, the chirp-type a.c. excitation signals typically had 1 V amplitude, 4-8 ms time length and 40–60 kHz bandwidth to fully cover the contact resonance peaks; the *a.c.* signals were superimposed on d.c. pulse switching waveforms within various bias windows up to ±30 V. Measured BE spectra were fitted to a simple harmonic oscillator model to extract intrinsic piezoresponse amplitude and phase signals of the STO:MgO thin films, as reported in the article. Spectroscopic mapping was performed by moving the tip over a dense grid of points evenly defined on a region of interest.

Phase field simulation. Phase-field modeling was performed using a self-developed module within the framework of a commercial finite-element method (FEM) software (Comsol Multiphysics v5.2). The detailed modeling parameters are available in the supporting information.

Acknowledgments

Author Contributions

Enriquez, Jia and Chen synthesized and characterized the thin films. Q. Li, and Kalinin worked on the PFM and phase field simulation. Bowlan, Taylor, Yarotski, and Prasankumar contributed to the SHG characterization. Lu, Zhang, Li, and Wang characterized the microstructure of thin films. All authors have given approval to the final version of the manuscript.

Conflicts of interest

There are no conflicts to declare.

References

1. Schlom, D. G.; Chen, L. Q.; Fennie, C. J.; Gopalan, V.; Muller, D. A.; Pan, X. Q.; Ramesh, R.; Uecker, R. *MRS Bull.* **2014,** 39, 118.
2. Choi, K. J.; Biegalski, M.; Li, Y. L.; Sharan, A.; Schubert, J.; Uecker, R.; Reiche, P.; Chen, Y. B.; Pan, X. Q.; Gopalan, V.; Chen, L. Q.; Schlom, D. G.; Eom, C. B. *Science* **2004,** 306, (5698), 1005-1009.
3. Schlom, D. G.; Chen, L. Q.; Eom, C. B.; Rabe, K. M.; Streiffer, S. K.; Triscone, J. M. *Annu. Rev. Mater. Res.* **2007,** 37, 589-626.
4. Jalan, B.; Allen, S. J.; Beltz, G. E.; Moetakef, P.; Stemmer, S. *Appl. Phys. Lett.* **2011,** 98, (13), 132102.
5. Guo, E.-J.; Desautels, R.; Keavney, D.; Roldan, M. A.; Kirby, B. J.; Lee, D.; Liao, Z.; Charlton, T.; Herklotz, A.; Zac Ward, T.; Fitzsimmons, M. R.; Lee, H. N. *Sci. Adv.* **2019,** 5, (3), eaav5050.
6. MaCmanus-Driscoll, J. L.; Zerrer, P.; Wang, H. Y.; Yang, H.; Yoon, J.; Fouchet, A.; Yu, R.; Blamire, M. G.; Jia, Q. X. *Nat. Mater.* **2008,** 7, (4), 314-320.
7. Chen, A. P.; Su, Q.; Han, H.; Enriquez, E.; Jia, Q. X. *Adv. Mater.* **2019,** 31, 1803241.
8. Chen, A. P.; Hu, J.-M.; Lu, P.; Yang, T. N.; Zhang, W.; Li, L.; Ahmed, T.; Enriquez, E.; Weigand, M.; Su, Q.; Wang, H. Y.; Zhu, J.-X.; MacManus-Driscoll, J. L.; Chen, L. Q.; Yarotski, D.; Jia, Q. X. *Sci. Adv.* **2016,** 2, e1600245.
9. Harrington, S. A.; Zhai, J. Y.; Denev, S.; Gopalan, V.; Wang, H. Y.; Bi, Z. X.; Redfern, S. A. T.; Baek, S. H.; Bark, C. W.; Eom, C. B.; Jia, Q. X.; Vickers, M. E.; MacManus-Driscoll, J. L. *Nature Nanotechnol.* **2011,** 6, (8), 491-495.

ARTICLE

10. Khatkhatay, F.; Chen, A. P.; Lee, J. H.; Zhang, W. R.; Abdel-Raziq, H.; Wang, H. Y. *ACS Appl. Mater. Interfaces* **2013,** 5, (23), 12541-12547.

11. Haeni, J. H.; Irvin, P.; Chang, W.; Uecker, R.; Reiche, P.; Li, Y. L.; Choudhury, S.; Tian, W.; Hawley, M. E.; Craigo, B.; Tagantsev, A. K.; Pan, X. Q.; Streiffer, S. K.; Chen, L. Q.; Kirchoefer, S. W.; Levy, J.; Schlom, D. G. *Nature* **2004,** 430, (7001), 758-761.

12. Irvin, P.; Levy, J.; Guo, R.; Bhalla, A. *Appl. Phys. Lett.* **2005,** 86, (4), 042903.

13. Ahadi, K.; Galletti, L.; Li, Y.; Salmani-Rezaie, S.; Wu, W.; Stemmer, S. *Sci. Adv.* **2019,** 5, (4), eaaw0120.

14. Choi, E.-M.; Di Bernardo, A.; Zhu, B.; Lu, P.; Alpern, H.; Zhang, K. H. L.; Shapira, T.; Feighan, J.; Sun, X.; Robinson, J.; Paltiel, Y.; Millo, O.; Wang, H.; Jia, Q.; MacManus-Driscoll, J. L. *Sci. Adv.* **2019,** 5, (4), eaav5532.

15. Bonilla, F. J.; Novikova, A.; Vidal, F.; Zheng, Y. L.; Fonda, E.; Demaille, D.; Schuler, V.; Coati, A.; Vlad, A.; Garreau, Y.; Simkin, M. S.; Dumont, Y.; Hidki, S.; Etgens, V. *ACS Nano* **2013,** 7, (5), 4022-4029.

16. Schuler, V.; Bonilla, F. J.; Demaille, D.; Coati, A.; Vlad, A.; Garreau, Y.; Sauvage-Simkin, M.; Novikova, A.; Fonda, E.; Hidki, S.; Etgens, V.; Vidal, F.; Zheng, Y. L. *Nano Research* **2015,** 8, (6), 1964-1974.

17. Ning, X.; Wang, Z.; Zhang, Z. *Adv. Funct. Mater.* **2014,** 24, (34), 5393-5401.

18. Cantoni, C.; Gao, Y. F.; Wee, S. H.; Specht, E. D.; Gazquez, J.; Meng, J. Y.; Pennycook, S. J.; Goyal, A. *ACS Nano* **2011,** 5, (6), 4783-4789.

19. Liu, H. J.; Liang, W. I.; Chu, Y. H.; Zheng, H. M.; Ramesh, R. *MRS Commun.* **2014,** 4, (2), 31-44.

20. Chen, A. P.; Bi, Z. X.; Jia, Q. X.; MacManus-Driscoll, J. L.; Wang, H. Y. *Acta Mater.* **2013,** 61, ( ), 2783.

21. Hsieh, Y. H.; Liou, J. M.; Huang, B. C.; Liang, C. W.; He, Q.; Zhan, Q.; Chiu, Y. P.; Chen, Y. C.; Chu, Y. H. *Adv. Mater.* **2012,** 24, (33), 4564-4568.

22. Chen, A. P.; Bi, Z. X.; Tsai, C. F.; Lee, J.; Su, Q.; Zhang, X. H.; Jia, Q. X.; MacManus-Driscoll, J. L.; Wang, H. Y. *Adv. Funct. Mater.* **2011,** 21, (13), 2423-2429.

23. Li, W. W.; Zhao, R.; Tang, R. J.; Chen, A. P.; Zhang, W. R.; Lu, X.; Wang, H. Y.; Yang, H. *ACS Appl. Mater. Interfaces* **2014,** 6, (8), 5356-5361.

24. Li, W.; Zhang, W.; Wang, L.; Gu, J.; Chen, A.; Zhao, R.; Liang, Y.; Guo, H.; Tang, R.; Wang, C.; Jin, K.; Wang, H.; Yang, H. *Sci. Rep.* **2015,** 5, 11335.

25. Hsieh, Y. H.; Strelcov, E.; Liou, J. M.; Shen, C. Y.; Chen, Y. C.; Kalinin, S. V.; Chu, Y. H. *ACS Nano* **2013,** 7, (10), 8627-8633.

26. Zhao, R.; Li, W. W.; Chen, A. P.; Zhang, W. R.; Yang, J.; Liang, Y.; Tang, R. J.; Wang, H. Y.; Yang, H. *Appl. Phys. Lett.* **2014,** 105, (7), 072907.

27. Cho, S.; Yun, C.; Tappertzhofen, S.; Kursumovic, A.; Lee, S.; Lu, P.; Jia, Q. X.; Fan, M.; Jian, J.; Wang, H. Y.; Hofmann, S.; MacManus-Driscoll, J. L. *Nat. Commun.* **2016,** 7, 12373.

28. Lee, S.; Sangle, A.; Lu, P.; Chen, A. P.; Zhang, W. R.; Lee, J. S.; Wang, H. Y.; Jia, Q. X.; MacManus-Driscoll, J. L. *Adv. Mater.* **2014,** 26, (36), 6284-6289.

29. Su, Q.; Yoon, D.; Chen, A. P.; Khatkhatay, F.; Manthiram, A.; Wang, H. Y. *J. Power Sources* **2013,** 242, 455-463.

30. Ma, W.; Kim, J. J.; Tsvetkov, N.; Daio, T.; Kuru, Y.; Cai, Z.; Chen, Y.; Sasaki, K.; Tuller, H. L.; Yildiz, B. *J. Mater. Chem. A* **2015,** 3, (1), 207-219.

31. Adamo, C.; Ke, X.; Wang, H. Q.; Xin, H. L.; Heeg, T.; Hawley, M. E.; Zander, W.; Schubert, J.; Schiffer, P.; Muller, D. A.; Maritato, L.; Schlom, D. G. *Appl. Phys. Lett.* **2009,** 95, (11), 112504.

32. Kan, D. S.; Shimakawa, Y. *Appl. Phys. Lett.* **2011,** 99, (8), 081907.

33. Chen, A. P.; Khatkhatay, F.; Zhang, W.; Jacob, C.; Jiao, L.; Wang, H. Y. *J. Appl. Phys.* **2013,** 114, (12), 124101.

34. Arredondo, M.; Ramasse, Q. M.; Weyland, M.; Mahjoub, R.; Vrejoiu, I.; Hesse, D.; Browning, N. D.; Alexe, M.; Munroe, P.; Nagarajan, V. *Adv. Mater.* **2010,** 22, (22), 2430-2434.

35. Uberuaga, B. P.; Dholabhai, P. P.; Pilania, G.; Chen, A. *Apl Mater* **2019,** 7, (10), 100904.

36. Mbatang, R.; Xue, D.; Enriquez, E.; Yuan, R.; Han, H.; Dowden, P.; Wang, Q.; Fohtung, E.; Xue, D.; Lookman, T.; Pennycook, S. J.; Chen, A. P. *Nanoscale* **2019,** 11, (15), 7364-7370.

37. Breckenfeld, E.; Shah, A. B.; Martin, L. W. *J. Mater. Chem. C* **2013,** 1, (48), 8052-8059.

38. Agrawal, P.; Guo, J.; Yu, P.; Hebert, C.; Passerone, D.; Erni, R.; Rossell, M. D. *Phys. Rev. B* **2016,** 94, 104101.

39. Chen, A. P.; Zhou, H. H.; Bi, Z. X.; Zhu, Y. Y.; Luo, Z. P.; Bayraktaroglu, A.; Phillips, J.; Choi, E. M.; MacManus-Driscoll, J. L.; Pennycook, S. J.; Narayan, J.; Jia, Q. X.; Zhang, X. H.; Wang, H. Y. *Adv. Mater.* **2013,** 25, (7), 1028-1032.

40. Li, X.; Qiu, T.; Zhang, J.; Baldini, E.; Lu, J.; Rappe, A. M.; Nelson, K. A. *Science* **2019,** 364, (6445), 1079-1082.

41. Pertsev, N.; Tagantsev, A.; Setter, N. *Phys Rev B* **2000,** 61, (2), R825.

42. Zhu, Y. Y.; Song, C. Y.; Minor, A. M.; Wang, H. Y. *Microsc. Microanal.* **2013,** 19, (3), 706-715.

43. Brooks, C.; Kourkoutis, L. F.; Heeg, T.; Schubert, J.; Muller, D.; Schlom, D. *Appl. Phys. Lett.* **2009,** 94, (16), 162905.

44. Groenen, R.; Smit, J.; Orsel, K.; Vailionis, A.; Bastiaens, B.; Huijben, M.; Boller, K.; Rijnders, G.; Koster, G. *APL Mater.* **2015,** 3, (7), 070701.

45. Morozovska, A.; Eliseev, E.; Tagantsev, A.; Bravina, S.; Chen, L.-Q.; Kalinin, S. *Phys Rev B* **2011,** 83, (19), 195313.

46. Wang, D.; Huang, C.; He, J.; Che, X.; Zhang, H.; Huang, F. J. A. o. **2017,** 2, (3), 1036-1039.

47. Mohaddes-Ardabili, L.; Zheng, H.; Zhan, Q.; Yang, S. Y.; Ramesh, R.; Salamanca-Riba, L.; Wuttig, M.; Ogale, S. B.; Pan, X. *Appl. Phys. Lett.* **2005,** 87, (20), 203110.

48. Li, Q.; Nelson, C. T.; Hsu, S. L.; Damodaran, A. R.; Li, L. L.; Yadav, A. K.; McCarter, M.; Martin, L. W.; Ramesh, R.; Kalinin, S. V. *Nature Commun.* **2017,** 8, (1), 1468.

49. Sheng, G.; Li, Y. L.; Zhang, J. X.; Choudhury, S.; Jia, Q. X.; Gopalan, V.; Schlom, D. G.; Liu, Z. K.; Chen, L. Q. *Appl. Phys. Lett.* **2010,** 96, (23), 232902.

50. Chen, L. Q. *J. Am. Ceram. Soc.* **2008,** 91, (6), 1835-1844.

51. Denev, S. A.; Lummen, T. T.; Barnes, E.; Kumar, A.; Gopalan, V. *J. Am. Ceram. Soc.* **2011,** 94, (9), 2699-2727.

52. Mishina, E. D.; Morozov, A. I.; Sigov, A. S.; Sherstyuk, N. E.; Aktsipetrov, O. A.; Lemanov, V. V.; Rasing, T. *Journal of Experimental and Theoretical Physics* **2002,** 94, (3), 552-567.

53. Grigas, J., *Microwave dielectric spectroscopy of ferroelectrics and related materials*. Routledge: 2019.

54. Sheu, Y.; Trugman, S.; Yan, L.; Chuu, C.-P.; Bi, Z.; Jia, Q.; Taylor, A.; Prasankumar, R. *Phys Rev B* **2013,** 88, (2), 020101.

55. Jang, H. W.; Kumar, A.; Denev, S.; Biegalski, M. D.; Maksymovych, P.; Bark, C. W.; Nelson, C. T.; Folkman, C. M.; Baek, S. H.; Balke, N.; Brooks, C. M.; Tenne, D. A.; Schlom, D. G.; Chen, L. Q.; Pan, X. Q.; Kalinin, S. V.; Gopalan, V.; Eom, C. B. *Phys. Rev. Lett.* **2010,** 104, (19), 197601.

56. Sangle, A. L.; Lee, O. J.; Kursumovic, A.; Zhang, W.; Chen, A.; Wang, H.; MacManus-Driscoll, J. L. *Nanoscale* **2018,** 10, (7), 3460-3468.